

**Direct numerical simulations of a microswimmer in a viscoelastic fluid**

Journal:	<i>Soft Matter</i>
Manuscript ID	SM-ART-05-2023-000600.R2
Article Type:	Paper
Date Submitted by the Author:	13-Aug-2023
Complete List of Authors:	Kobayashi, Takuya; Kyoto University, Department of Chemical Engineering Jung, Gerhard; CNRS Montpellier Matsuoka, Yuki; Sumitomo Bakelite Co Ltd, Nakayama, Yasuya; Kyushu University, Department of Chemical Engineering Molina, John; Kyoto University, Department of Chemical Engineering Yamamoto, Ryoichi; Kyoto University, Department of Chemical Engineering

Cite this: DOI: 00.0000/xxxxxxxxxx

Direct numerical simulations of a microswimmer in a viscoelastic fluid

Takuya Kobayashi,^a Gerhard Jung,^{a,b} Yuki Matsuoka,^c Yasuya Nakayama,^d John J. Molina^a and Ryoichi Yamamoto^{*a}

Received Date

Accepted Date

DOI: 00.0000/xxxxxxxxxx

This study presents the application of the smoothed profile (SP) method to perform direct numerical simulations for the motion of both passive and active “squirming” particles in Newtonian and viscoelastic fluids. We found that fluid elasticity has a significant impact on both the transient behavior and the steady-state velocity of the particles. Specifically, we observe that the swirling flow generated by the squirmer’s surface velocity significantly enhances their swimming speed as the Weissenberg number increases, regardless of the swimming type. Furthermore, we find that pushers outperform pullers in Oldroyd-B fluids, suggesting that the speed of a squirmer depends on the swimmer type. To understand the physical origin of the phenomenon of swirling flow enhancing the swimming speed, we investigate the velocity field and polymer conformation around non-swirling and swirling neutral squirmers in viscoelastic fluids. Our investigation reveals that the velocity field around the neutral swirling squirmers exhibits pusher-like extensional flow characteristics, as well as an asymmetric polymer conformation distribution, which gives rise to this increased propulsion. This is confirmed by the investigation of the force on a fixed squirmer, which revealed that the polymer stress, particularly its diagonal components, plays a critical role in enhancing the swimming speed of swirling squirmers in viscoelastic fluids. Additionally, our results demonstrate that the maximum swimming speeds of swirling squirmers occur at an intermediate value of the fluid viscosity ratio for all swimmer types. These findings have important implications for understanding the behavior of particles and micro-organisms in complex fluids.

1 Introduction

Self-propelled particles are naturally exposed to complex or crowded fluid environments.¹ Examples with high industrial and biological relevance are bacteria in biofilms or polymeric solutions,² as well as spermatozoa in cervical mucus.³ These viscoelastic environments are fundamentally different from purely viscous Newtonian fluids because they exhibit solid- or liquid-like behaviour, depending on the imposed rate of deformation. In equilibrium systems, this already leads to fascinating dynamical properties, e.g., allowing a person to walk on “water”.⁴ For self-propelled particles, the effect of viscoelasticity becomes even more pronounced, because the motion of the particles crucially affects the emerging steady-state properties such as the motility-induced phase separation.⁵ Experimental results also indicate an

enhancement of rotational diffusion in viscoelastic fluids which can lead to spontaneous symmetry breaking and subsequent circular motion for spherical active particles.⁶ Moreover, experimental and numerical studies found viscoelastic fluids promote the collective swimming of sperm cells,^{7,8} indicating that fluid elasticity promotes collective behavior.

Despite the relevance of studying self-propelled particles in viscoelastic fluids and promising experimental results, most computational studies in the field of “wet” active particles have focused on Newtonian fluids.⁹ The reason is that the incorporation of viscoelasticity requires more complex numerical integrators, particularly to determine the frequency-dependent coupling of the active particle with the fluctuating complex fluid while maintaining the required boundary conditions on the surface of the colloid. Recently, however, there have been several numerical investigations of self-propelled particles in viscoelastic fluids, demonstrating an enhancement of rotational diffusion,¹⁰ an enhancement in the swimming speed caused by swirling,^{11,12} an increase in the aggregation of pushers suspensions,¹³ and a decrease in the rate of working with increasing fluid elasticity.¹⁴

In this study, we have extended the smoothed profile (SP)

^a Department of Chemical Engineering, Kyoto University, Kyoto 615-8510, Japan. E-mail: ryoichi@cheme.kyoto-u.ac.jp

^b Laboratoire Charles Coulomb (L2C), Université de Montpellier, CNRS, 34095 Montpellier, France.

^c Corporate Engineering Center, Sumitomo Bakelite Co., Ltd., Shizuoka 426-0041, Japan.

^d Department of Chemical Engineering, Kyushu University, Fukuoka 819-0395, Japan.

method^{15,16} to simulate swimming particles in viscoelastic fluids. The SP method is a highly efficient direct numerical simulation method that fully resolves the hydrodynamic coupling between fluid and particles, enabling us to calculate multi-particle systems.¹⁶ The SP method has been successfully used to study suspensions of self-propelled particles in Newtonian fluids^{17–22} and passive particles in viscoelastic fluids.^{23,24} Here, we extend it for the first time to investigate suspensions of self-propelled particles in viscoelastic fluids. To the best of our knowledge, there have been limited reports on numerical investigations of a suspension of active particles in viscoelastic fluids in three dimensions.^{25,26} We focus on a single active particle systems in this work, but the SP method we have developed can easily simulate dense dispersions. In particular, we have conducted direct numerical simulations of both passive and active particles in Oldroyd-B fluids. We performed an error analysis of the numerical procedure, investigated the steady-state velocities of individual sedimenting and swimming particles, and compared them to the analytical results. To understand the swimming speed enhancement observed for swirling swimmers in viscoelastic fluids, we analyzed the velocity and polymer conformation fields around the squirmers in Oldroyd-B fluids. Finally, to gain deeper insight into the mechanism behind this enhancement of the swimming speed, we computed the different contributions to the force on a fixed swirling squirmer in an Oldroyd-B fluid.

2 Viscoelastic model

The equations of motion for the three-dimensional fluid velocity field \mathbf{u}_f are given by,

$$\rho \left(\frac{\partial}{\partial t} + \mathbf{u}_f \cdot \nabla \right) \mathbf{u}_f = \nabla \cdot \boldsymbol{\sigma} \quad (1)$$

$$\nabla \cdot \mathbf{u}_f = 0 \quad (2)$$

where ρ is the (constant) fluid density, and where we have assumed incompressibility.

The stress tensor $\boldsymbol{\sigma} = \boldsymbol{\sigma}_s + \boldsymbol{\sigma}_p$ consists of two contributions. The first is the pressure and viscous contribution $\boldsymbol{\sigma}_s = -p\mathbf{I} + \eta_s \mathbf{D}$, where η_s is the solvent viscosity and $\mathbf{D} = \nabla \mathbf{u}_f + (\nabla \mathbf{u}_f)^T$ is the deformation tensor. The second is the polymeric stress contribution $\boldsymbol{\sigma}_p$, defined in terms of the polymer conformation tensor \mathbf{C} , which in this work is given by the Oldroyd-B constitutive equation,

$$\left(\frac{\partial}{\partial t} + \mathbf{u}_f \cdot \nabla \right) \mathbf{C} = (\nabla \mathbf{u}_f)^T \cdot \mathbf{C} + \mathbf{C} \cdot (\nabla \mathbf{u}_f) - \frac{\mathbf{C} - \mathbf{I}}{\lambda} \quad (3)$$

$$\boldsymbol{\sigma}_p = \frac{\eta_p}{\lambda} (\mathbf{C} - \mathbf{I}) \quad (4)$$

where η_p describes the polymeric contribution to the shear viscosity and $\eta_0 = \eta_s + \eta_p$ is the effective zero-frequency shear viscosity. In contrast to the viscous contribution, the polymeric contribution is governed by a finite relaxation time λ , over which the polymeric conformation tensor is relaxing towards its equilibrium configuration $\mathbf{C}_{\text{eq}} = \mathbf{I}$. The general time-dependence of this deformation tensor is defined in Eq. (3).

3 Simulation method

In this work, we employed the smoothed profile (SP) method^{15,16} to resolve the fluid-particle coupling. Rather than relying on a pure (Lagrangian) particle-based approach, like the smoothed particle hydrodynamics (SPH) method, or a (Eulerian) mesh-based approach, like the finite-element method (FEM), the SP method uses a hybrid representation that allows for the calculation of both fluid and particle properties on a fixed Cartesian grid. This allows us to attain a high computational efficiency. The SP method is similar to the fluid particle dynamics (FPD) method,²⁷ which represents particles as highly viscous fluids. However, FPD only enforces the particle rigidity approximately, the exact limit corresponding to an infinite fluid particle viscosity. This approximation imposes a numerical challenge, as higher viscosities require smaller integration time steps to achieve accurate simulations. In contrast, the SP method treats colloidal particles as non-deformable solids, i.e., directly enforcing the particle rigidity through an additional constraint force in the Navier-Stokes equation.¹⁵

The (spherical) particles follow the Newton-Euler equations

$$\dot{\mathbf{R}}_i = \mathbf{V}_i \quad \dot{\mathbf{Q}}_i = \text{skew}(\boldsymbol{\Omega}_i) \cdot \mathbf{Q}_i \quad (5)$$

$$M_i \dot{\mathbf{V}}_i = \mathbf{F}_i^{\text{H}} + \mathbf{F}_i^{\text{other}} \quad \mathbf{I}_i \cdot \dot{\boldsymbol{\Omega}}_i = \mathbf{N}_i^{\text{H}} + \mathbf{N}_i^{\text{other}} \quad (6)$$

with \mathbf{R}_i and \mathbf{V}_i the centre-of-mass position and velocity, \mathbf{Q}_i and $\boldsymbol{\Omega}_i$ the orientation matrix and angular velocity, and $M_i = M = 4\pi a^3 \rho_p / 3$ and $\mathbf{I}_i = 2Ma^2 \mathbf{I} / 5$ (\mathbf{I} the unit tensor) the mass and moment of inertia for particle i , respectively, where we have assumed spherical particles of equal radii a and mass density ρ_p . The forces \mathbf{F} (torques \mathbf{N}) have been decomposed into hydrodynamic \mathbf{F}^{H} and other $\mathbf{F}^{\text{other}}$ contributions, respectively, where the latter can include direct particle-particle or external forces. The function $\text{skew}(\boldsymbol{\Omega}_i)$ is used to create the skew-symmetric matrix of the angular velocity $\boldsymbol{\Omega}_i$, defined as:

$$\text{skew}(\boldsymbol{\Omega}) = -\varepsilon_{ijk} \Omega_k \mathbf{e}_i \otimes \mathbf{e}_j \quad (7)$$

$$= \begin{pmatrix} 0 & -\Omega_z & \Omega_y \\ \Omega_z & 0 & -\Omega_x \\ -\Omega_y & \Omega_x & 0 \end{pmatrix} \quad (8)$$

where ε_{ijk} is the Levi-Civita symbol.

The basic idea of the SP method is to model the (rigid) particles as immersed “fluid” particles that are rendered rigid by imposing a constraint force. The particles can be described by a (smoothed) phase field function ϕ , thus removing the explicit and cumbersome treatment of the particle surfaces, and making the generalization to many-body systems trivial. Within the SP method, the

evolution of the total velocity field \mathbf{u} is given by,

$$\rho \left(\frac{\partial}{\partial t} + \mathbf{u} \cdot \nabla \right) \mathbf{u} = \nabla \cdot \boldsymbol{\sigma} + \rho \phi \mathbf{f}_p \quad (9)$$

$$\mathbf{u} = (1 - \phi) \mathbf{u}_f + \phi \mathbf{u}_p \quad (10)$$

$$\phi \mathbf{u}_p = \sum_i \phi_i [\mathbf{V}_i + \boldsymbol{\Omega}_i \times \mathbf{r}_i] \quad (11)$$

Here, the hydrodynamic force density $\rho \phi \mathbf{f}_p$, required to maintain the particle rigidity, is chosen such that momentum conservation is exactly satisfied. The particle velocity field is calculated using the individual rigid particle contributions, defined in terms of their translational \mathbf{V}_i and angular velocities $\boldsymbol{\Omega}_i$, and the particle's smooth profile or phase-field function ϕ_i (with $\mathbf{r}_i = \mathbf{x} - \mathbf{R}_i$ the relative distance from the particle center to the field position \mathbf{x}).

In the present study, we used a ϕ_i defined as¹⁵

$$\phi_i(\mathbf{x}) = g(|\mathbf{x} - \mathbf{R}_i|) \quad (12)$$

$$g(x) = \frac{h[(a + \xi/2) - x]}{h[(a + \xi/2) - x] + h[x - (a - \xi/2)]} \quad (13)$$

$$h(x) = \begin{cases} \exp(-\Delta^2/x^2) & x \geq 0 \\ 0 & x < 0 \end{cases} \quad (14)$$

where \mathbf{R}_i , a , ξ and Δ are the position of the particle, the radius of the particle, the interfacial thickness, and the grid spacing, respectively.

3.1 DNS method for viscoelastic fluids

To numerically solve for the hydrodynamics, we first update the polymer stress $\boldsymbol{\sigma}_p$ using the Oldroyd-B constitutive equation. However, while the \mathbf{C} tensor should be positive definite, a discretized integrator for \mathbf{C} following Eq. (3) does not necessarily guarantee the positive definiteness is maintained. In fact, numerical instabilities induced by fluctuations will render the conformation tensor not positive-definite.²⁸ Thus, instead of working directly with $\boldsymbol{\sigma}_p$, we use the more stable representation in terms of the contravariant deformation tensor \mathbf{b} , such that $\mathbf{C} = \mathbf{b} \cdot \mathbf{b}^T$, thereby guaranteeing that the reconstructed confirmation tensor \mathbf{C} is always positive definite by definition.²⁸

Within the \mathbf{b} -representation, the Oldroyd-B model is given by²⁹

$$\left(\frac{\partial}{\partial t} + \mathbf{u} \cdot \nabla \right) \mathbf{b} = (\nabla \mathbf{u})^T \cdot \mathbf{b} - \frac{\mathbf{b} - \mathbf{b}^{-T}}{2\lambda} \quad (15)$$

where $\mathbf{b}^{-T} = (\mathbf{b}^T)^{-1} = (\mathbf{b}^{-1})^T$. We update the contravariant deformation tensor \mathbf{b} over the interval $(t_n, t_{n+1} = t_n + \Delta t)$, as follows:

$$\mathbf{b}^{n+1} = \mathbf{b}^n + \int_{t_n}^{t_{n+1}} ds \left[(\nabla \mathbf{u})^T \cdot \mathbf{b} - \frac{\mathbf{b} - \mathbf{b}^{-T}}{2\lambda} - \nabla \cdot (\mathbf{b} \mathbf{u}) \right] \quad (16)$$

After this, the updated \mathbf{b} is converted into the conformation tensor $\mathbf{C} = \mathbf{b} \cdot \mathbf{b}^T$, and the updated polymer stress $\boldsymbol{\sigma}_p$ is computed using Eq. (4).

Next, we use the fractional step approach¹⁵ to update the total

velocity \mathbf{u} . We integrate Eq. (9) without the body force $\rho \phi \mathbf{f}_p$ term, to yield an intermediate velocity field \mathbf{u}^* as follows:

$$\mathbf{u}^* = \mathbf{u}^n + \int_{t_n}^{t_{n+1}} ds \nabla \cdot \left[\rho^{-1} (\boldsymbol{\sigma}_s + \boldsymbol{\sigma}_p) - \mathbf{u} \mathbf{u} \right] \quad (\nabla \cdot \mathbf{u}^* = 0) \quad (17)$$

Simultaneously, the particle positions and orientations are updated according to

$$\mathbf{R}_i^{n+1} = \mathbf{R}_i^n + \int_{t_n}^{t_{n+1}} ds \mathbf{V}_i \quad (18)$$

$$\mathbf{Q}_i^{n+1} = \mathbf{Q}_i^n + \int_{t_n}^{t_{n+1}} ds \text{skew}(\boldsymbol{\Omega}_i) \cdot \mathbf{Q}_i \quad (19)$$

We assume momentum conservation to calculate the hydrodynamic force and torque on the particle, which are given by the momentum exchange between fluid and particle domains, as

$$\int_{t_n}^{t_{n+1}} ds \mathbf{F}_i^H = \int d\mathbf{x} \rho \phi_i^{n+1} (\mathbf{u}^* - \mathbf{u}_p^n) \quad (20)$$

$$\int_{t_n}^{t_{n+1}} ds \mathbf{N}_i^H = \int d\mathbf{x} \left[\mathbf{r}_i^{n+1} \times \rho \phi_i^{n+1} (\mathbf{u}^* - \mathbf{u}_p^n) \right] \quad (21)$$

We then calculate the updated particle velocities \mathbf{V}_i^{n+1} and $\boldsymbol{\Omega}_i^{n+1}$ from the hydrodynamic and other contributions,

$$\mathbf{V}_i^{n+1} = \mathbf{V}_i^n + M^{-1} \int_{t_n}^{t_{n+1}} ds (\mathbf{F}_i^H + \mathbf{F}_i^{\text{other}}) \quad (22)$$

$$\boldsymbol{\Omega}_i^{n+1} = \boldsymbol{\Omega}_i^n + \mathbf{I}^{-1} \cdot \int_{t_n}^{t_{n+1}} ds (\mathbf{N}_i^H + \mathbf{N}_i^{\text{other}}) \quad (23)$$

Finally, the total velocity \mathbf{u} is expressed as

$$\mathbf{u}^{n+1} = \mathbf{u}^* + \int_{t_n}^{t_{n+1}} ds \phi \mathbf{f}_p \quad (\nabla \cdot \mathbf{u}^{n+1} = 0) \quad (24)$$

$$\int_{t_n}^{t_{n+1}} ds \phi \mathbf{f}_p = \phi^{n+1} (\mathbf{u}_p^{n+1} - \mathbf{u}^*) \quad (25)$$

Numerically, we have used an Adams-Bashforth method (with an Euler update for the first step) to integrate the contravariant deformation tensor and the particle equations of motions. The updated velocity field \mathbf{u}^* is obtained from a first order exponential time-difference algorithm within the vorticity representation, $\boldsymbol{\omega} = \nabla \times \mathbf{u}$, the remaining particle constraint force is obtained from a first-order Euler method. We note that we enforce the incompressibility constraint whenever the fluid velocity field is updated. This can be understood as coming from an intermediate pressure gradient term; alternatively, this can be done by taking the Fourier transform of the velocity and projecting out the components of $\hat{\mathbf{u}}$ parallel to \mathbf{k} ,

$$\hat{\mathbf{u}} \rightarrow \left[\mathbf{I} - \frac{\mathbf{k}\mathbf{k}}{k^2} \right] \cdot \hat{\mathbf{u}} \quad (26)$$

Further details can be found in Ref.¹⁶.

3.2 DNS method for microswimmers

We use the squirmer model developed by Lighthill³⁰ and Blake³¹ to represent microswimmers. This mathematical model, orig-

inally developed to represent the ciliary propulsion of microorganisms, has been widely adopted as the canonical model to investigate hydrodynamic interactions of microswimmers,^{11,32–34} including within the SP method.^{17–22} The propulsion is generated by imposing a modified stick boundary condition at the surface of the particle, the general form of which is given by³⁵

$$\mathbf{u}^{\text{sq}} = \sum_{n=1}^{\infty} \frac{2}{n(n+1)} B_n P'_n(\cos \theta) \sin \theta \boldsymbol{\theta} + \sum_{n=1}^{\infty} C_n P'_n(\cos \theta) \sin \theta \boldsymbol{\phi} \quad (27)$$

where P'_n is the derivative of the n -order Legendre polynomial, B_n and C_n are the coefficients for the n -th polar and azimuthal squirmering modes, and $\boldsymbol{\theta}$ and $\boldsymbol{\phi}$ are the unit tangent vectors in the polar and azimuthal directions, respectively.

In most studies, only the first two polar modes, B_1 and B_2 in Eq. (27), are considered, as B_1 determines the steady state swimming speed in a Newtonian fluid ($U_N = 2/3B_1$), and the ratio of the two $\alpha = B_2/B_1$ determines the swimmer type (pusher, puller, or neutral). Swimmers with $\alpha < 0$ are called pushers, as they create an extensile flow, reminiscent of a pushing motion (e.g. sperm cells, *E.coli.* and most bacteria), while $\alpha > 0$ denotes pullers (e.g. *Chlamydomonas*), which create a contractile flow. Squirmers with $\alpha = 0$ are called neutral swimmers, which generate a potential flow.

Recently, several works have considered the effect of the azimuthal modes for swimming in complex fluids.^{11,12,36} The swirling flow generated by these azimuthal modes was shown to lead to an increase in the swimming speed of a squirmer in a viscoelastic fluid^{11,12} and a decrease in a shear-thinning fluid,³⁶ as compared to swimming in a Newtonian fluid. In the present study, we will consider the first two polar modes (B_1 and B_2) and the second azimuthal mode C_2 , which result in the following simplified expression for the surface slip velocity

$$\mathbf{u}^{\text{sq}} = B_1 \left[\left(\sin \theta + \frac{\alpha}{2} \sin 2\theta \right) \boldsymbol{\theta} + \frac{3}{2} \zeta \sin 2\theta \boldsymbol{\phi} \right] \quad (28)$$

where $\zeta = C_2/B_1$ denotes the magnitude of the swirling.

We now present the computational algorithm for simulating these squirmers within viscoelastic fluids, analogous to the Newtonian fluid implementation.¹⁷ To account for the hydrodynamics of the squirmering motion, defined by the surface slip velocity \mathbf{u}^{sq} in Eq. (28), we have added a squirmer body force $\rho \phi \mathbf{f}_{\text{sq}}$ term to the modified Navier-Stokes equation, such that Eq. (9) becomes

$$\rho \left(\frac{\partial}{\partial t} + \mathbf{u} \cdot \nabla \right) \mathbf{u} = \nabla \cdot \boldsymbol{\sigma} + \rho \phi \mathbf{f}_p + \rho \phi \mathbf{f}_{\text{sq}} \quad (29)$$

For this, we adapt the same fractional step approach described in Section. 3.1. First, we update the polymer stress $\boldsymbol{\sigma}_p$ (Eqs. (16) and (4)), the intermediate (total) velocity \mathbf{u}^* (Eq. (17)), and the particle positions \mathbf{R}_i (orientations \mathbf{Q}_i) (Eqs. (18) and (19)). We then integrate the squirmer body force term $\rho \phi \mathbf{f}_{\text{sq}}$ to update the

total velocity field \mathbf{u}^{**} as follows,

$$\begin{aligned} \mathbf{u}^{**} &= \mathbf{u}^* + \int_{t_n}^{t_{n+1}} ds \phi \mathbf{f}_{\text{sq}} \quad (\nabla \cdot \mathbf{u}^{**} = 0) \quad (30) \\ \int_{t_n}^{t_{n+1}} ds \phi \mathbf{f}_{\text{sq}} &= \sum_{i=1}^N \phi_i^{\text{sq}} (\mathbf{V}_i + \boldsymbol{\Omega}_i \times \mathbf{r}_i + \mathbf{u}_i^{\text{sq}} - \mathbf{u}^*) \\ &\quad + \sum_{i=1}^N \phi_i (\delta \mathbf{V}_i + \delta \boldsymbol{\Omega}_i \times \mathbf{r}_i) \quad (31) \end{aligned}$$

The first term on the right-hand side of Eq. (31) imposes the slip velocity \mathbf{u}^{sq} at the surface of the squirmer; where $\phi_i^{\text{sq}} = (1 - \phi_i) |\nabla \phi_i| / \max(|\nabla \phi|)$ is a smoothed surface function which is non-zero only within the interfacial domain of the particle. This represents the force/momentum that the swimmer exerts on the fluid (e.g., due to the movement of the cilia at the surface of the swimmer). Thus, to maintain momentum conservation, and account for the counter-force exerted by the fluid on the particle, we must also include the second term on the right-hand side of Eq. (31), which adds a counter-flow within the particle domain that exactly balances the momentum given to the fluid to impose the squirmering velocity \mathbf{u}^{sq} . This secondary flow is defined in terms of the changes to the rigid-particle velocity $\delta \mathbf{V}_i$ and angular velocity $\delta \boldsymbol{\Omega}_i$.

The hydrodynamic force and torque on the particle are defined the same way as in Eqs. (20) and (21)

$$\int_{t_n}^{t_{n+1}} ds (\mathbf{F}_i^{\text{H}} + \mathbf{F}_i^{\text{sq}}) = \int d\mathbf{x} \rho \phi_i^{n+1} (\mathbf{u}^{**} - \mathbf{u}_p^n) \quad (32)$$

$$\int_{t_n}^{t_{n+1}} ds (\mathbf{N}_i^{\text{H}} + \mathbf{N}_i^{\text{sq}}) = \int d\mathbf{x} [\mathbf{r}_i^{n+1} \times \rho \phi_i^{n+1} (\mathbf{u}^{**} - \mathbf{u}_p^n)] \quad (33)$$

The updated particle velocities \mathbf{V}_i^{n+1} and $\boldsymbol{\Omega}_i^{n+1}$, now including the squirmer contributions, are calculated from these forces and torques. We note that the squirmering or slip velocity should be imposed with respect to the particle velocities at the end of the time-step $\mathbf{V}_i^{n+1}, \boldsymbol{\Omega}_i^{n+1}$ (Eq.(31)), however, at that point of our numerical scheme these updated particle velocities are unknown. This means that the surface velocity profile at the end of the time-step is not necessarily the correct one. Thus, we employ an iterative scheme, which repeatedly solves Eqs.(31-33) until convergence is reached for these particle velocities (see Ref.¹⁷ for further details).

Finally, we can determine the total velocity \mathbf{u} using the following equations, which are similar to Eqs. (24) and (25)

$$\mathbf{u}^{n+1} = \mathbf{u}^{**} + \int_{t_n}^{t_{n+1}} ds \phi \mathbf{f}_p \quad (\nabla \cdot \mathbf{u}^{n+1} = 0) \quad (34)$$

$$\int_{t_n}^{t_{n+1}} ds \phi \mathbf{f}_p = \phi^{n+1} (\mathbf{u}_p^{n+1} - \mathbf{u}^{**}) \quad (35)$$

4 Velocity of sedimenting particles and microswimmers in viscoelastic fluids

In this section we analyze the transient and steady-state swimming speed of particles immersed in viscoelastic fluids. Our study

includes sedimenting passive particles, non-swirling microswimmers and finally, microswimmers with swirl. To set the stage, we start by investigating sedimenting particles in a Newtonian fluid.

4.1 A sedimenting particle in a Newtonian fluid

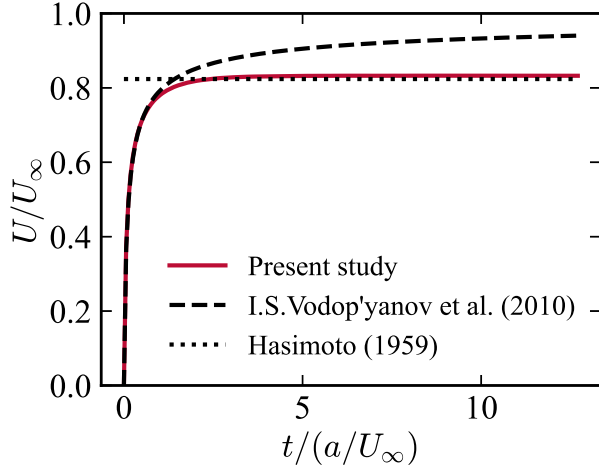


Fig. 1 The transient sedimentation velocity of a particle with radius $a = 4\Delta$, within a Newtonian fluid, in a periodic cubic simulation box of length $L = 64\Delta$. The dashed and dotted lines indicate the Vodop'yanov *et al.* solution³⁷ and the approximate solution by Hasimoto,³⁸ respectively. The sedimentation velocity agrees with the former (Eq. (37)) at the beginning of the sedimentation, and with the latter (Eq. (40)) at the steady state. The sedimentation velocity U and time t are scaled by the Stokes velocity U_∞ and the associated time-scale a/U_∞ , respectively.

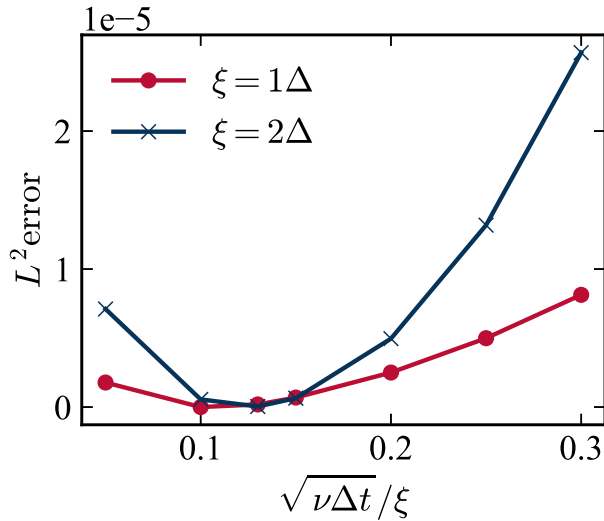


Fig. 2 The error in the steady-state velocity of a particle (radius $a = 4\Delta$) sedimenting in a Newtonian fluid, as a function of $\sqrt{v\Delta t}/\xi$. The red circles and blue crosses correspond to results for an interface thickness of $\xi = 1\Delta$ and 2Δ , respectively. Our SP method simulation results were compared to the semi-exact solution of Hasimoto (Eq. (40)),³⁸ and the error was found to be a non-monotonic function of $\sqrt{v\Delta t}/\xi$.³⁹ This error is minimized for an optimal time increment Δt , which depends on the interface thickness ξ and the kinematic viscosity of the fluid ν .

First, we simulate the sedimentation of a particle in a New-

tonian fluid and validate our numerical method by comparing our simulation results to the analytical solutions given by Vodop'yanov *et al.*³⁷ and Hasimoto.³⁸ The simulations were conducted in a cubic simulation box of length $L = 64\Delta$, where Δ is the grid spacing. For the SP simulation parameters, we set the radius of the particle as $a = 4\Delta$ and the interfacial thickness as $\xi = 2\Delta$, and the density ratio between the particle and the fluid was $\rho_p/\rho = 1.1$. To prevent the whole fluid from drifting in the direction of gravity under periodic boundary conditions, a counteracting pressure gradient is imposed on the system in order to ensure momentum conservation. This is achieved by setting the $\mathbf{k} = \mathbf{0}$ mode of the velocity field to be null, $\hat{\mathbf{u}}(\mathbf{k} = \mathbf{0}) = \int d\mathbf{r} \mathbf{u} = \mathbf{0}$. The equation of motion for a particle settling in an unbounded fluid, at small Reynolds numbers, is described by

$$\frac{4}{3}\pi a^3 \rho_p \frac{dU}{dt} = -\frac{2}{3}\pi a^3 \rho \frac{dU}{dt} + \frac{4}{3}\pi a^3 (\rho_p - \rho)g - 6\pi\eta aU - 6a^2\sqrt{\pi\rho\eta} \int_0^t \frac{U(t')}{\sqrt{t-t'}} dt' \quad (36)$$

with η the viscosity. For a density ratio of $\rho_p/\rho = 1.1$, the solution of Eq. (36) is given by Vodop'yanov *et al.*³⁷

$$\frac{U}{U_\infty} = 1 + \frac{2}{\sqrt{\pi(8-5\rho/\rho_p)}} \text{Im} \left(\frac{1}{\zeta} \Phi \left(\frac{9\eta\zeta^2 t}{\rho_p a^2} \right) \right) \quad (37)$$

where $U_\infty = 2(\rho_p - \rho)a^2g/9\eta$ is the Stokes velocity of a settling particle, and Φ and ζ are given by,

$$\Phi(z) = \int_z^\infty \frac{e^{-\zeta}}{\sqrt{\zeta}} \frac{d\zeta}{\sqrt{\zeta}} = 2e^z \int_{\sqrt{z}}^\infty e^{-x^2} dx \quad (38)$$

$$\zeta^2 = \frac{|4 - 7\rho/\rho_p| + 3i\sqrt{\rho/\rho_p(5\rho/\rho_p - 8)}}{2(\rho/\rho_p + 2)^2} \quad (39)$$

For the specific case of a particle sedimenting in a periodic cubic box, the steady-state sedimentation velocity is given by Hasimoto as,³⁸

$$\frac{U}{U_\infty} = 1 - 1.7601c^{\frac{1}{3}} + c - 1.5593c^2 + O(c^{\frac{5}{3}}) \quad (40)$$

where c is the particle volume fraction.

Fig. 1 shows the transient sedimentation velocity of the particle, as given by our SP method simulation results, as well as the analytical solutions of Vodop'yanov *et al.* (Eq. (37)) and the approximate solution of Hasimoto (Eq. (40)). Our results for the transient behavior at the beginning of the sedimentation are in good agreement with the former and coincide with the latter at the steady state, as required.

To quantify the accuracy of our simulation results, we compute the error in the steady-state sedimentation velocity, with respect to the semi-exact solution of Hasimoto (Eq. (40)). Fig. 2 shows this error, as a function of $\sqrt{v\Delta t}/\xi$,³⁹ where $\nu = \eta/\rho$ is the kinematic viscosity. These results were obtained for a particle of radius $a = 4\Delta$ and two different values of the interfacial thicknesses ξ (1Δ and 2Δ). We found that the error is a non-monotonic function of the step size, and is minimized for an optimal time increment Δt , which depends on the interfacial thickness ξ and the

kinematic viscosity ν .

4.2 A sedimenting particle in an Oldroyd-B fluid

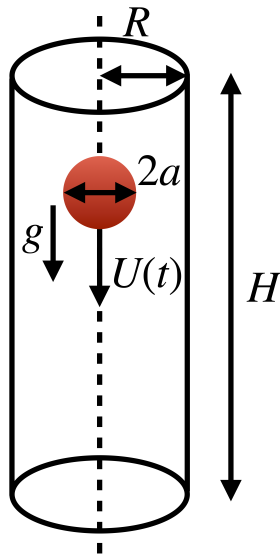


Fig. 3 A schematic illustration of the setup used to simulate the sedimentation of a particle (radius a) under gravity (acceleration g), within an Oldroyd-B fluid, in a cylindrical container (radius R , height H).

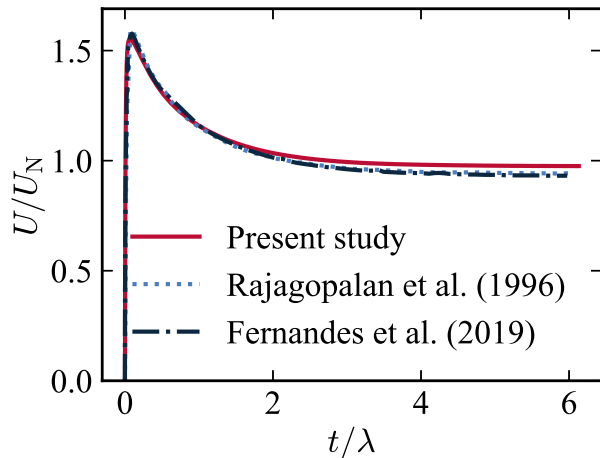


Fig. 4 The transient motion of a particle of radius $a = 8\Delta$ through an Oldroyd-B fluid in the pipe of height $H = 512\Delta$. The red solid line, blue dotted line, and black dash-dotted line represent the results obtained in the present study, those of Rajagopalan *et al.*⁴⁰ and those of Fernandes *et al.*,⁴¹ respectively. Our simulation results for the transient sedimentation velocity of a particle are consistent with the results obtained by Rajagopalan *et al.*⁴⁰ and Fernandes *et al.*⁴¹ The sedimentation velocity U is scaled by the theoretical Newtonian sedimentation velocity U_N , the time t is scaled by the relaxation time λ of the polymer conformation.

Next, we verify the accuracy of the SP method for simulating a sedimenting particle in an Oldroyd-B fluid. For this, we conducted simulations for a particle of radius $a = 8\Delta$ and interfacial thickness $\xi = 2\Delta$, within a cylindrical pipe of height $H = 512\Delta$ and radius $R/a = 4.115$ (see Fig. 3). The pipe is represented as an assembly of fixed rigid particles, of the same dimensions as the particle.

We apply periodic boundary conditions along the axis aligned with the pipe's axis of symmetry. The time step Δt is the optimal value for the corresponding Newtonian system, determined by the interfacial thickness ξ and the kinematic viscosity ν (see Fig. 2). The Reynolds number is $Re = 2a\rho U_N/\eta_0 = 0.064$, where U_N is the steady Newtonian sedimentation velocity in the pipe, the Weissenberg number is $Wi = \lambda U_N/a = 2.45$, and the viscosity ratio is $\beta = \eta_s/\eta_0 = 0.59$. The transient velocity for a particle sedimenting within an Oldroyd-B fluid in this cylindrical domain is shown in Fig. 4. These results clearly illustrate the fluid elasticity effects on the sedimentation velocity. In particular, at the beginning of the sedimentation, a velocity overshoot is observed. This phenomenon can be attributed to the time delay between the fluid deformation and the corresponding stress that occurs in a viscoelastic fluid. Our results are in good agreement with the numerical results of Rajagopalan *et al.*⁴⁰ and Fernandes *et al.*⁴¹ This indicates that the SP method accurately couples the hydrodynamics of particles in both Newtonian and Oldroyd-B fluids.

4.3 Microswimmers in an Oldroyd-B fluid

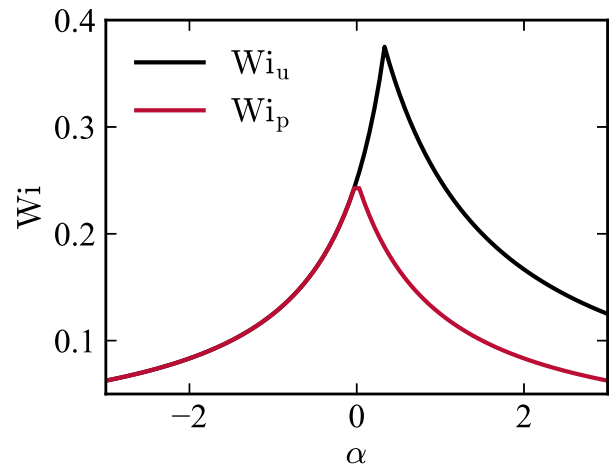


Fig. 5 Upper limit of validity for the UCM/Oldroyd-B models, Wi_u (black), and the radius of convergence of the series solution, Wi_p (red) as a function of the swimming strength α .¹²

We now consider the ability of the SP method to simulate swimmers in viscoelastic fluids. Here, we must take special care regarding the range of validity of the model. In particular, Housiadas *et al.*¹² have demonstrated that for squirmers in Upper Convected Maxwell (UCM) and Oldroyd-B fluids, the polymer stress σ_p at the poles of the particles can diverge. This is due to the specific uniaxial and biaxial elongational flows generated at the poles. Fortunately, Housiadas *et al.* have also provided both the upper limit for the validity of the exact solution Wi_u , together with the radius of convergence of the series solution Wi_p , for the polymer stress at the poles, as a function of the swimming strength α (Fig. 5). Furthermore, this singularity is found to depend strongly on the swimming strength α . Thus, the limit for the physically valid range of Weissenberg numbers, when solving for the poly-

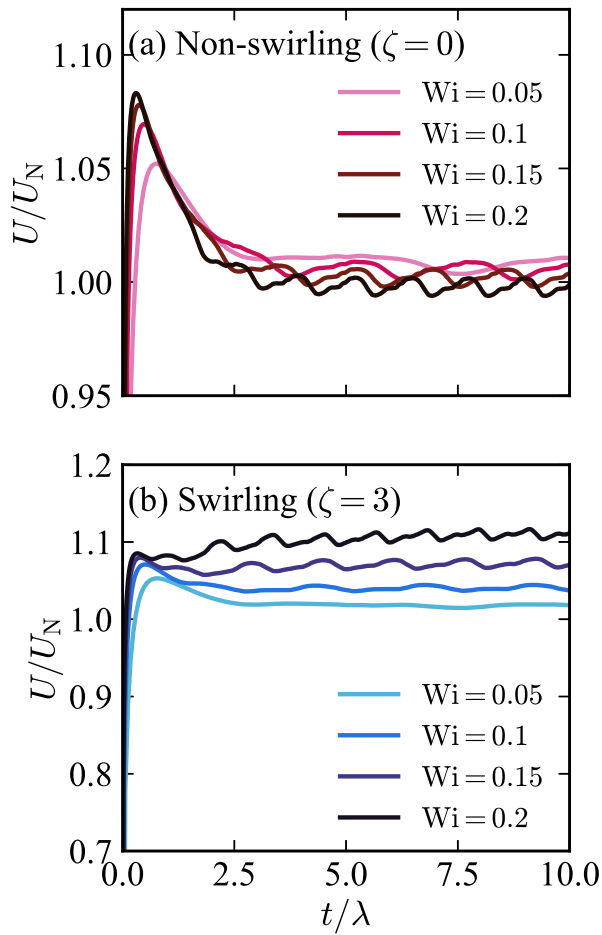


Fig. 6 Swimming speeds of (a) a non-swirling ($\zeta = 0$) and (b) a swirling ($\zeta = 3$) neutral squirmer, with a radius of $a = 6\Delta$, in an Oldroyd-B fluid, within a periodic cubic simulation box of length $L = 64\Delta$, at $Re = 0.01$. The swimming speed U is scaled by the Newtonian swimming speed U_N obtained using the SP method, and the time t is scaled by the relaxation time λ .

mer stress at the poles of a squirmer, is given by¹²

$$0 \leq Wi < Wi_u = \begin{cases} \frac{1}{4(1-\alpha)} & (\alpha \leq \frac{1}{3}) \\ \frac{1}{2(1+\alpha)} & (\alpha > \frac{1}{3}) \end{cases} \quad (41)$$

In addition, when perturbation methods are used to solve the polymer stress at the north and south poles of a squirmer, the radius of convergence Wi_p for the series solution is given by¹²

$$Wi_p = \begin{cases} \frac{1}{8} & (\alpha = \pm 1) \\ \frac{1}{4} \min\left(\frac{1}{|1+\alpha|}, \frac{1}{|1-\alpha|}\right) & (\alpha \neq \pm 1) \end{cases} \quad (42)$$

This solution converges for $0 \leq Wi < Wi_p$. Based on these findings, the use of squirmer particles in UCM and Oldroyd-B models is limited to very small Weissenberg numbers, which represent weakly elastic fluids.¹² Fig. 5 indicates that Wi_u is always greater

than or equal to Wi_p . Therefore, in this study, we investigate the range of $0 \leq Wi < Wi_p$. For instance, for $\alpha = 0$ and ± 1 , the valid range is $0 \leq Wi < 0.25$ and $0 \leq Wi < 0.125$, respectively. To validate the SP method, we have performed simulations for a single neutral squirmer ($\alpha = 0$) in an Oldroyd-B fluid. The simulations were conducted in a cubic simulation box of length $L = 64\Delta$. We used a particle radius of $a = 6\Delta$ and an interfacial thickness of $\xi = 2\Delta$. The Reynolds number $Re = \rho a U_N / \eta_0$ ($U_N = 2/3B_1$ the steady Newtonian swimming speed) is 0.01 and the viscosity ratio $\beta = \eta_s / \eta_0$ is 0.5. To quantify the effects of the swirling, we will consider swimmers with $\zeta = 0, 3$. Fig. 6 shows the transient swimming speed for a neutral squirmer ($\alpha = 0$). The speed of the swirling swimmer ($\zeta = 3$) is seen to increase with the Weissenberg number $Wi = \lambda B_1 / a$, whereas that of the non-swirling swimmer ($\zeta = 0$) is essentially independent of Wi .

In Fig. 6(a), an overshoot in the swimming speed of non-swirling squirmers is observed in the transient regime $t/\lambda \lesssim 1$ for all Wi . This is similar to the overshoot observed in the sedimentation velocity, as shown in Fig. 4. In contrast, Fig. 6(b) shows that for swirling squirmers, this overshoot is only observed for $Wi \lesssim 0.1$, and is dampened compared to the non-swirling case. This suggests that the swirling flow leads to a swimming speed enhancement, resulting in a steady state velocity that is larger than the overshoot velocity of a non-swirling squirmer, thus masking the overshoot mechanism.

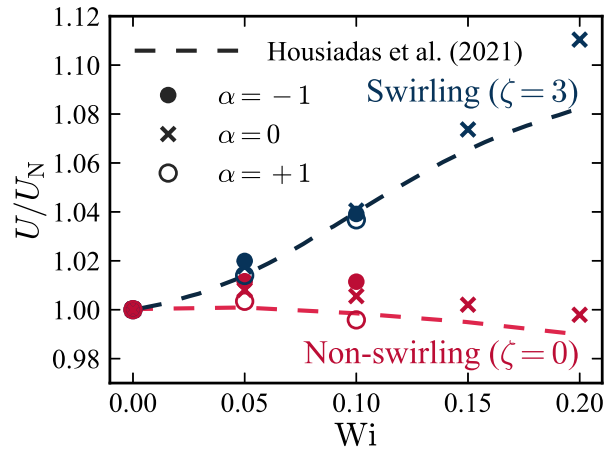


Fig. 7 Swimming speeds for pushers ($\alpha = -1$, filled circles), pullers ($\alpha = 1$, empty circles) and neutral swimmers ($\alpha = 0$, crosses) in the steady state, for a viscosity ratio $\beta = 0.5$, as a function of the Weissenberg number $Wi = \lambda B_1 / a$. The red and blue data correspond to the non-swirling ($\zeta = 0$) and swirling cases ($\zeta = 3$), respectively. The dashed lines show the numerical results for a neutral squirmer ($\alpha = 0$) obtained by Housiadas *et al.*¹² Our predicted swimming speeds U are scaled by the Newtonian swimming speed U_N obtained using the SP method.

To investigate the effects of α , which determines the swimming type, we have calculated the steady-state swimming speeds U for pusher ($\alpha = -1$), puller ($\alpha = 1$), and neutral ($\alpha = 0$) swimmers (for the same swirling parameters $\zeta = 0, 3$). As shown in Fig. 7, a swirling squirmer always swims faster than a non-swirling one for $Wi > 0$, regardless of α . Furthermore, this swimming velocity enhancement, caused by the swirling flow, is greater for swimmers

with larger values of α . Finally, for the case of a neutral swimmer, we can compare our results with the simulation results of Housiadas *et al.*¹² However, we note that their simulation conditions are not exactly the same as ours. In particular, they consider a swimmer within a periodic cylindrical channel (radius $R/a = 20$, length $L/a = 40$), whereas we have used a fully periodic cubic simulation box (length $L/a \simeq 10.7$). Nevertheless, as shown in Fig. 7, we obtain very good agreement with their numerical results. We consider that the small deviations between these two sets of numerical results are primarily due to the difference in the boundary condition setups. In any case, these differences ($\simeq 3\%$) are of the same order of magnitude as the expected error of using a diffuse particle interface, as reported by Molina *et al.*¹⁷ for the swimming speed of squirmers in Newtonian fluids.

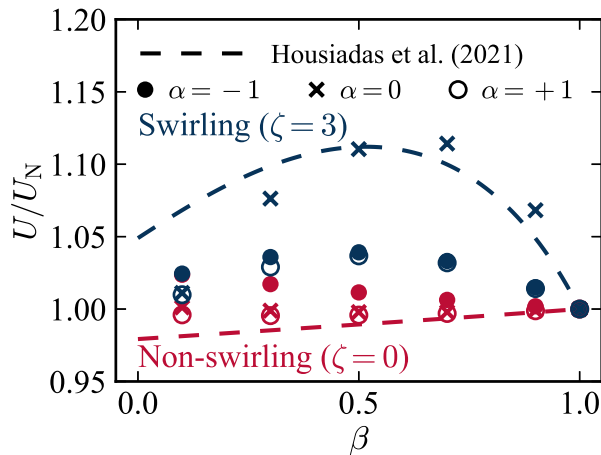


Fig. 8 Swimming speeds for pushers ($\alpha = -1$, filled circles), pullers ($\alpha = 1$, empty circles), and neutral squirmers ($\alpha = 0$, crosses) as a function of the viscosity ratio $\beta = \eta_s/\eta_0$. The Weissenberg number is $Wi = 0.1$ for the pushers and pullers, and $Wi = 0.2$ for the neutral squirmer. The red and blue data correspond to non-swirling ($\zeta = 0$) and swirling cases ($\zeta = 3$), respectively. The dashed lines show the approximate solution for a neutral squirmer ($\alpha = 0$) obtained by Housiadas *et al.*¹² Our predicted swimming speeds U are scaled by the Newtonian swimming speed U_N obtained using the SP method.

To quantify the dependence of the swimming speed on the viscosity ratio β , we performed additional simulations, varying the viscosity ratio β within the range $[0.1, 1.0]$, for a neutral squirmer at Weissenberg number $Wi = 0.2$, and a pusher and a puller at $Wi = 0.1$. Fig. 8 shows the swimming speeds U for neutral squirmers ($\alpha = 0$), pushers ($\alpha = -1$), and pullers ($\alpha = 1$), as a function of the viscosity ratio β , for both swirling ($\zeta = 3$) and non-swirling ($\zeta = 0$) swimmers. In the swirling case, we observe a non-monotonic dependence of U with respect to β , with all swimmer types exhibiting a higher velocity compared to the non-swirling one, with a maximum at an intermediate β ($\sim 1/2$ for pushers and pullers, $\sim 3/4$ for neutral swimmers). The results for the neutral swimmers are in good quantitative agreement with the approximate solution of Housiadas *et al.*,¹² in both the magnitude of the enhancement and the location of the peak. We note that a similar trend is also observed in a Giesekus fluid.¹¹ In contrast, for the non-swirling cases, the changes in the velocity are

much weaker, and exhibit a more complex dependence on α and β . While pushers show a slow monotonic decrease in the velocity, as a function of β , the velocity for pullers and neutral swimmers remains essentially constant, although for pullers there is a very weak increase with β .

5 Influence of viscoelasticity on swimming speed

In the previous section, we noted the nontrivial phenomena related to change in swimming speed of both passive and active particles in viscoelastic fluids. In the following, we will further analyze this behavior, and study the role played by the polymer stretching and the elasticity.

5.1 Comparing sedimenting and active particles

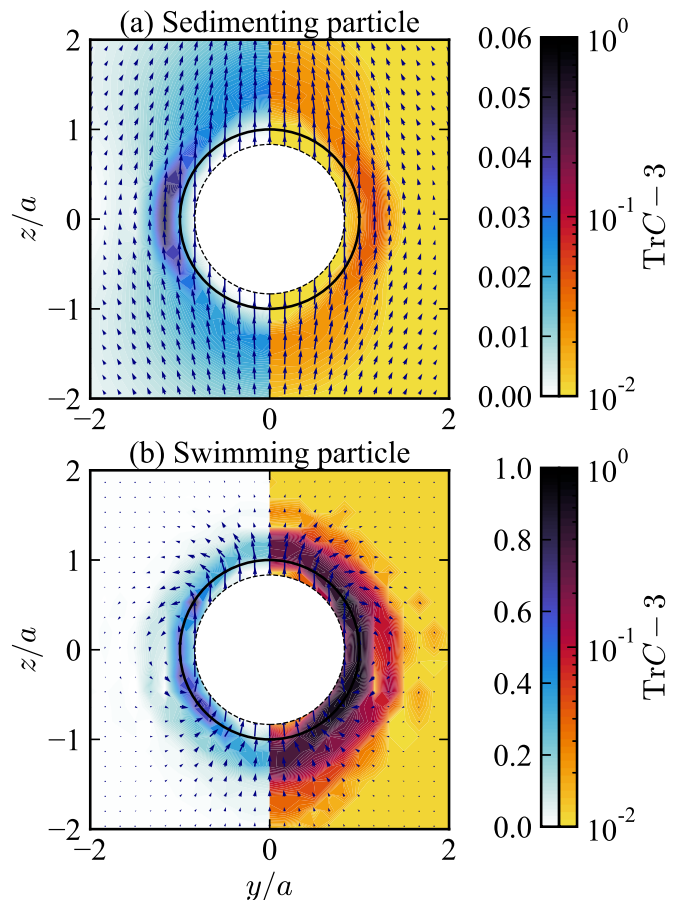


Fig. 9 Velocity field and the trace of the conformation tensor $\text{Tr}\mathbf{C} - 3$ around (a) a sedimenting (passive) particle and (b) a swimming particle, specifically non-swirling neutral squirmers ($\alpha = \zeta = 0$) for $Re = \rho a U_N / \eta_0 = 0.01$, $Wi = \lambda B_1 / a = 0.2$, and a viscosity ratio $\beta = \eta_s / \eta_0 = 0.5$, in the steady state. The blue and red color bars represent the trace of the conformation tensor in linear and logarithmic scales, respectively. The ranges of the linear (blue) color bars differ between the (a) passive particle and (b) neutral squirmer, while the ranges of the logarithmic (orange) color bars the same. The magnitude of the trace of the conformation tensor around a squirmer is significantly higher than that around a sedimenting particle.

We first consider the velocity field, and the trace of the conformation tensor $\text{Tr}\mathbf{C} - 3 = C_{xx} + C_{yy} + C_{zz} - 3$ around both a sed-

imining particle and a swimming particle, specifically, a non-swirling neutral squirmer ($\alpha = \zeta = 0$). Both particles were set to have the same steady-state velocity in the Stokes regime. For the sedimenting particle, this is achieved by setting the sedimenting velocity U to the swimming velocity of a squirmer for $\text{Re} = \rho a U_N / \eta_0 = 0.01$ and $\text{Wi} = \lambda B_1 / a = 0.2$, using Eq. (40). Comparing Figs. 4 and 6, we have previously found that both particles show very similar properties in the transient flow and the steady-state swimming speed.

In Fig. 9, we visualize the magnitude of the trace of the conformation tensor and the velocity profile at steady-state. We find that the polymer stretching is larger in magnitude, but also much more localized for a squirmer than for a passive particle. These differences in magnitude and localization are attributed to the differences in the flow profiles, which decay as $\sim r^{-1}$ and $\sim r^{-3}$ for passive particles and neutral squirmers, respectively. This strong and highly localized degree of polymer stretching indicates that squirmers are more susceptible to the influence of viscoelasticity compared to passive particles, with implications for microswimmer suspensions¹³.

5.2 Comparing non-swirling and swirling microswimmers

To better understand the mechanism underlying why swirling squirmers swim faster than non-swirling ones in viscoelastic fluids, we investigate the velocity field and the trace of the conformation tensor TrC around both non-swirling and swirling neutral squirmers. As shown in Fig. 10, the velocity field around the swirling squirmer is noticeably different than the one generated by non-swirling squirmers. In particular, in the presence of swirling, the velocity field resembles that of a pusher, i.e., an extensional-like flow, with a stagnation point at the rear of the particle. Fig. 11 shows that the flow field generated by swirling (neutral) squirmers exhibits a slower decay ($\sim r^{-2}$) than that of non-swirling (neutral) squirmers ($\sim r^{-3}$). Additionally, we observe that the polymers near the swirling squirmer show a much stronger degree of extension than those of non-swirling squirmers, as illustrated in Fig. 10. This enhanced stretching, attributed to the ζ term, is also asymmetric, with a larger magnitude around the lower hemisphere ($z/a < 0$) than in the upper hemisphere ($z/a > 0$). This asymmetric stretching gives rise to an elastic force on the squirmer, resulting in the enhanced swimming speed. As depicted in Fig. 12, both the magnitude of the stretching and the degree of head-tail asymmetry increase with Wi . This explains the strong Wi dependence of the velocity field, which recovers the pusher-like extensional flow characteristics at higher Weissenberg numbers ($\text{Wi} \gtrsim 0.1$).

We now analyze the elastic force by calculating the force parallel to the swimming axis acting on a fixed neutral squirmer. As shown in Fig. 13, the total force increases with the Weissenberg number Wi , as does the swimming speed. To analyze this increase, we decompose the total force into the contributions coming from the squirming motion, solvent, and polymer. Fig. 13 demonstrates that the force contributions due to the polymer increase with the Weissenberg number Wi , whereas the solvent contribution remains roughly constant, and the swimming contribu-

tion shows a non-monotonic decrease with Wi . Therefore, we can conclude that the polymer contribution is the primary mechanism responsible for the swimming speed enhancement. The force contributions become nonlinear within the range of $0.15 \leq \text{Wi} \leq 0.2$, indicating that the swirling Weissenberg number ($\text{Wi}^{\text{swirl}} = \lambda \partial_r u_\phi$) exceeds a value of 1. Furthermore, we decompose the polymer contribution into its diagonal F^D and off-diagonal F^O components. Assuming the swimming axis is aligned with the z axis,

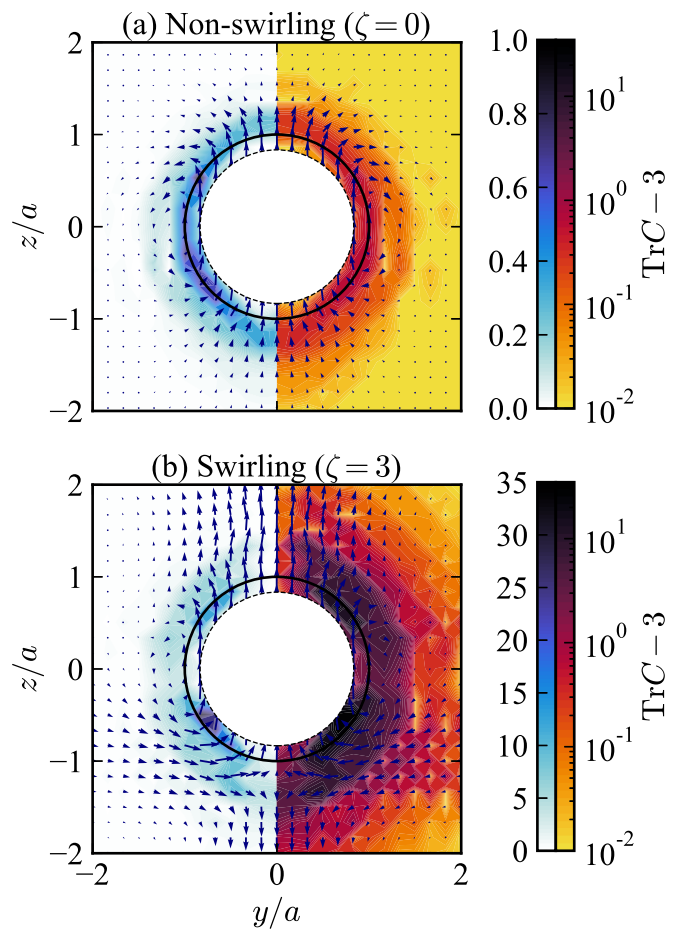


Fig. 10 Velocity field and the trace of the conformation tensor $\text{TrC} - 3$ around (a) non-swirling ($\zeta = 0$) and (b) swirling ($\zeta = 3$) neutral squirmers ($\alpha = 0$) in the steady state for a Weissenberg number $\text{Wi} = 0.2$ and a viscosity ratio $\beta = 0.5$. The blue and red color bars represent the trace of the conformation tensor in linear and logarithmic scales, respectively. The ranges of the linear color bars (blue) differ between the (a) non-swirling and (b) swirling squirmers, while the ranges of the logarithmic color bars (red) are the same. The velocity field around a swirling neutral squirmer differs from that around a non-swirling squirmer. Additionally, the magnitude of the trace of the conformation tensor around a swirling squirmer is significantly higher than that around a non-swirling squirmer.

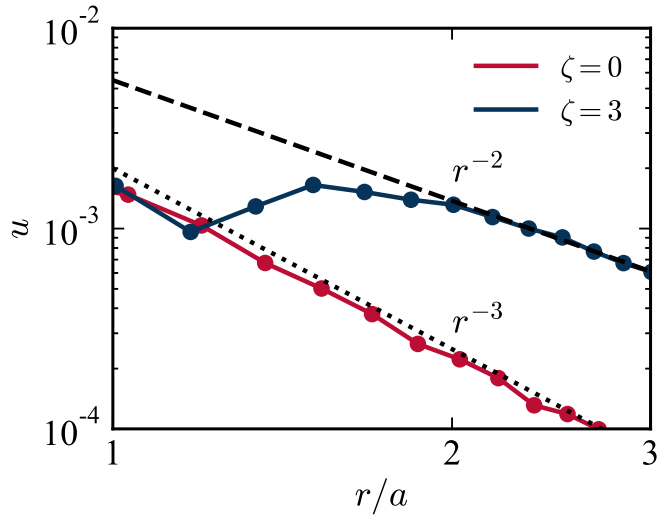


Fig. 11 Magnitude of the velocity u along the swimming direction, averaged over both swimming directions, $z/a > 0$ and $z/a < 0$, as a function of distance r/a , for both non-swirling ($\zeta = 0$) and swirling ($\zeta = 3$) neutral squirmers. The flow field of the swirling squirmer exhibits a slower decay ($\sim r^{-2}$) than that of the non-swirling squirmer ($\sim r^{-3}$).

we have

$$F^{\text{Polymer}} = \int_S (\boldsymbol{\sigma}_p \cdot d\mathbf{S})_z \quad (43)$$

$$= \int_V (\nabla \cdot \boldsymbol{\sigma}_p)_z dV \quad (44)$$

$$= \int_V \frac{\partial \sigma_{p,zz}}{\partial z} dV + \int_V \frac{\partial \sigma_{p,xz}}{\partial x} + \frac{\partial \sigma_{p,yz}}{\partial y} dV \quad (45)$$

$$= F^{\text{D}} + F^{\text{O}} \quad (46)$$

Fig. 14 shows that the contribution of the diagonal component F^{D} increases with the Weissenberg number Wi , while the off-diagonal contribution F^{O} decreases with Wi . Consequently, the polymer contribution to the total force increases with the Weissenberg number Wi due to the corresponding rise in the diagonal component of the polymer stress. We can conclude that the additional deformations of the polymers due to the swirling motion of a squirmer lead to the swimming speed enhancement.

6 Discussions

To validate our numerical method, we performed simulations of the sedimentation of a particle in both Newtonian and Oldroyd-B fluids, as well as a squirmer in an Oldroyd-B fluid. We compared our simulation results to both analytical solutions and numerical simulations from previous studies and found that our results obtained using the smoothed profile (SP) method are in good agreement with them.

For a sedimenting particle in a cylindrical pipe filled with an Oldroyd-B fluid, we observed an overshoot in the sedimentation velocity at the beginning of the sedimentation in Fig. 4. This overshoot is not observed in a Newtonian fluid as depicted in Fig. 1. The difference in transient velocity of a sedimenting particle can be attributed to fluid elasticity, which causes a time delay between

fluid deformation and the corresponding stress. As a particle sediments, it generates a flow field in the opposite direction, which results in the stretch and orientation of the conformation around a particle. In a viscoelastic fluid, the time delay between the flow deformation and the corresponding stress causes an overshoot in the velocity of a sedimenting particle. Therefore, the drag coefficient at the beginning of the sedimentation is smaller than at the steady state in a viscoelastic fluid.

In an Oldroyd-B fluid, fluid elasticity affects the swimming speed of both non-swirling and swirling squirmers, as shown in Fig. 6. For a non-swirling squirmer, we also observed an overshoot in the swimming speed at the beginning of the swimming in Fig. 6(a), as well as the velocity of a sedimenting particle in Fig. 4, due to the time delay between fluid deformation and the corresponding stress. The magnitude of the overshoot in the swimming speed increases with Wi , corresponding to longer relaxation times λ . In contrast, for swirling squirmers, the coupling between fluid elasticity and swirling flow leads to an enhanced steady-state swimming speed, which increases with Wi , such that the overshoot is no longer observed at $Wi = 0.2$. The enhanced swimming is consistent with the results of Binagia *et al.*¹¹ and Housiadas *et al.*¹² This phenomenology induced by the rotational-translational coupling is reminiscent of recent experiments with artificial microswimmers in viscoelastic fluids⁶ and simulations in polymeric suspensions.¹⁰

We investigated the effect of α , which determines the swimming type, on the swimming speed of squirmers in an Oldroyd-B fluid, and found that a swirling squirmer consistently outperforms a non-swirling one, irrespective of the swimming type, as shown in Fig. 7. The swirling flow created by the squirmer's surface velocity enhances the swimming speed of all swimmer types (pusher, puller and neutral squirmer) in an Oldroyd-B fluid. In a Newtonian fluid ($Wi = 0$), the swimming speeds of pushers ($\alpha = -1$), pullers ($\alpha = 1$) and neutral swimmers ($\alpha = 0$) are nearly the same, regardless of α and ζ , which is consistent with the relation $U/U_N \simeq 1 - 0.15\alpha Re$ obtained by Wang *et al.*⁴² However, in a viscoelastic fluid, the various flow fields generated by different types of squirmers influence the swimming speeds. Furthermore, this enhancement in the swimming velocity due to the swirling flow is more significant for swimmers with larger α values. Among all swimmer types, the puller experiences the most significant impact of the coupling between fluid elasticity and swirling flow on the swimming speed.

We also investigated the effect of the viscosity ratio β and observed that for all swimmer types, the swimming speeds of swirling squirmers are maximum for an intermediate value of the viscosity ratio ($\beta \simeq 1/2$ for pushers/pullers, $\beta \simeq 3/4$ for neutral swimmers) in Fig. 8. The swimming speed dependence of neutral squirmers, as a function of the viscosity ratio β , is consistent with the numerical results obtained in a Giesekus fluid by Binagia *et al.*¹¹ and the approximate solution obtained by Housiadas *et al.*¹² For all swimmer types, the trends can be attributed to the counterbalance between the viscous and elastic contribution. Pushers with swirl swim faster than pullers with swirl for all ranges of viscosity ratio ($[0.1, 1.0]$). On the other hand, the swimming speeds of non-swirling puller ($\alpha = 1$) and neutral ($\alpha = 0$) squirmers are

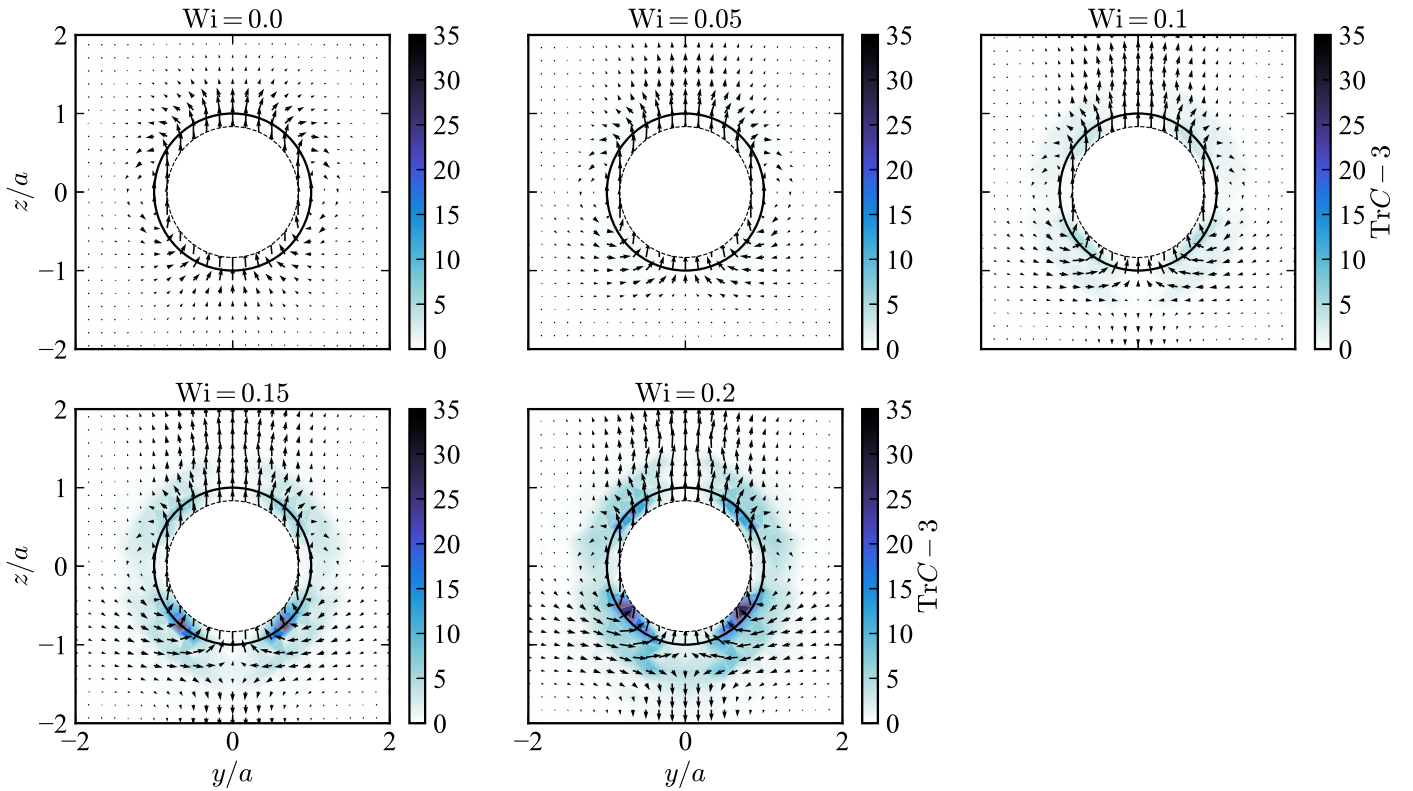


Fig. 12 Velocity field and the trace of the conformation tensor $\text{Tr}\mathbf{C} - 3$ around swirling neutral squirmers ($\alpha = 0$, $\zeta = 3$) in the steady state for various Wi and a viscosity ratio $\beta = 0.5$. The velocity field exhibits variations with different Weissenberg numbers Wi . For higher Wi , the velocity field resembles extensional flow fields along the swimming axis. The magnitude of the trace of the conformation tensor around a swirling squirmer increases with Wi . Furthermore, the increase in magnitude is more pronounced in the lower hemisphere ($z/a < 0$) than in the upper hemisphere ($z/a > 0$).

relatively independent of the viscosity ratio, while the swimming speed of a non-swirling pusher ($\alpha = -1$) increases with the viscosity ratio β . Thus, the swimmer type significantly affects the dependence of the swimming speed of a non-swirling squirmer on the viscosity ratio in a viscoelastic fluid.

We also found that, for the range of α and β investigated in this study, pushers outperform pullers at a finite Reynolds number, regardless of the presence of swirling. In fact, the difference in swimming speeds (at low Reynolds numbers) between pushers and pullers is greater in viscoelastic fluids than in Newtonian fluids, indicating a stronger coupling between fluid elasticity and flow field for pushers.

Moreover, we investigated the polymer conformation around a free neutral squirmer and the force on a fixed neutral squirmer. Our investigations revealed that as Wi increases, the asymmetric distribution of $\text{Tr}\mathbf{C}$ between the upper and lower hemispheres becomes more pronounced for the swirling squirmers, as shown in Fig. 12. Consequently, the polymer contribution to the force on a fixed neutral squirmer also increases with increasing Wi , as shown in Fig. 13. We discovered that the polymer stress, specifically its diagonal component, plays a crucial role in enhancing the swimming speed, as depicted in Figs. 13 and 14. Our findings are consistent with those of Housiadas *et al.*, who found that the pressure contribution is the major mechanism behind the swimming speed enhancement, by calculating the force on a free squirmer.¹²

7 Concluding remarks

We have utilized the smoothed profile (SP) method to perform direct numerical simulations of the motion of particles and swimmers in both Newtonian and viscoelastic fluids. By comparing our simulation results with analytical solutions and previous numerical simulations, we have validated the accuracy of the SP method. Our simulation results indicate that fluid elasticity significantly affects the transient behavior and steady-state velocity of particles and squirmers. In particular, the swirling flow generated by the squirmer's surface velocity enhances their swimming speed, leading to a remarkable increase in the swimming velocity with the Weissenberg number for all swimmer types. Additionally, we have found that pushers outperform pullers in Oldroyd-B fluids for both non-swirling and swirling squirmers, indicating that the swimming speed of a non-swirling squirmer depends on the swimmer type. Moreover, we have discovered that the maximum swimming speeds of swirling squirmer occur at an intermediate value of the viscosity ratio for all swimmer types.

We conducted a detailed investigation of the velocity and polymer conformation fields around a neutral squirmer. The velocity fields exhibit notable differences between non-swirling and swirling squirmers. Particularly, for higher Wi , the velocity field around the swirling (neutral) squirmer resembles the extensional flow fields generated by pushers. This flow field exhibits a slower decay ($\sim r^{-2}$) than the flow decay of non-swirling (neutral)

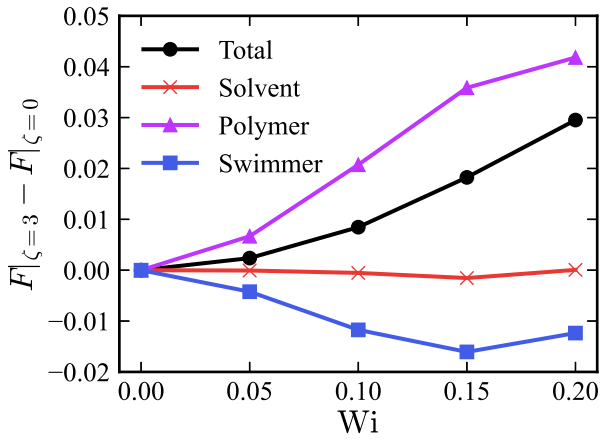


Fig. 13 Force difference between a swirling and non-swirling fixed neutral squirmer in an Oldroyd-B fluid for a viscosity ratio $\beta = 0.5$, as a function of the Weissenberg number Wi . The forces parallel to the swimming axis are shown, shifted by the value of the force on a non-swirling neutral squirmer ($\zeta = \alpha = 0$). The total force (black circle) increases with the Weissenberg number Wi , as does the swimming speed (Fig. 7). This is in contrast to the force contribution due to the solvent (red cross) and squirming motion (blue square), which both do not increase with the Weissenberg number Wi , but in accordance with the polymer contribution (purple triangle), which increases with Wi . Therefore, it is clear that the polymer contribution is responsible for the observed swimming speed enhancement.

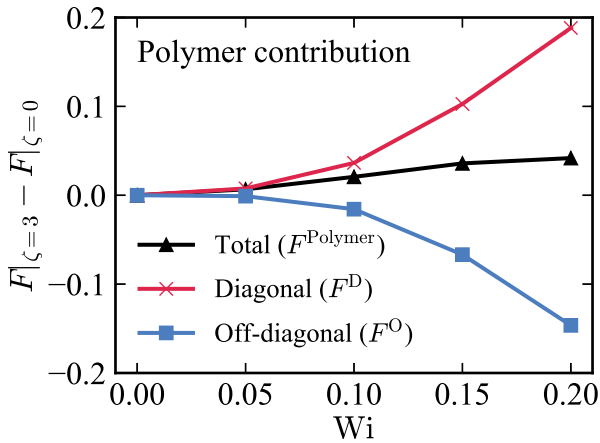


Fig. 14 Force difference between a swirling and non-swirling squirmer due to the diagonal (red cross) and off-diagonal (blue square) components of the polymer stress σ_p for a viscosity ratio $\beta = 0.5$, as a function of the Weissenberg number Wi . The force due to the diagonal component increases with the Weissenberg number Wi , while the off-diagonal component decreases with Wi . Therefore, the force due to the diagonal component of the polymer stress σ_p is crucial for the observed swimming speed enhancement.

squirmer ($\sim r^{-3}$). This (extensional) flow, generated by the stretching of the polymers, is expected to exert a strong influence on the collective behavior of squirmer suspensions due to its pronounced non-local nature. Our investigation of the polymer stretching highlights a significant difference in the trace of the conformation tensor between non-swirling and swirling squirmers in viscoelastic fluids. In particular, for swirling squirmers, the

trace of the conformation tensor is non-symmetric between the lower and upper hemispheres. This asymmetry induces an elastic force on the particle (in the propulsion direction), giving rise to the enhanced swimming speed of swirling squirmers, as well as the pusher-like extensional flow field.

Furthermore, we revealed that as Wi increases, the asymmetric distribution of the polymer conformation between the upper and lower hemispheres becomes more pronounced for the swirling squirmers. Consequently, the polymer contribution to the force also increases with increasing Wi . We discovered that the polymer stress, particularly its diagonal components, plays a critical role in enhancing the swimming speed.

With the UCM and Oldroyd-B fluids we have studied, the polymer stress at the poles of a squirmer becomes singular at a critical Weissenberg number Wi . This singularity, which arises from the divergence of the polymer stress σ_p in elongational flows, severely limits the parameter ranges that can be accessed using these models. However, by selecting a fluid in which the stress does not diverge under any deformation, it will be possible to calculate the behavior of a squirmer in a viscoelastic fluid for any Weissenberg number Wi . Our approach allows for such investigations into the behavior of squirmers in arbitrarily complex viscoelastic fluids, for which it can be challenging to obtain analytical results.

Our findings have important implications for understanding the behavior of particles and micro-organisms in complex fluids. Future studies should focus on investigating the underlying mechanism behind the swimming speed enhancement caused by swirling and the swimmer type difference in the swimming speed in a viscoelastic fluid.

Acknowledgements

This work was supported by the Grants-in-Aid for Scientific Research (JSPS KAKENHI) under grant nos. JP 20H00129, 20H05619, 20K03786, JP18K03563 and JP23K03343, and by JST SPRING, grant no. JPMJSP2110. G.J. acknowledges support by a short-term postdoctoral fellowship (JSPS PE21004).

Notes and references

- 1 J. Elgeti, R. G. Winkler and G. Gompper, *Reports on progress in physics*, 2015, **78**, 056601.
- 2 A. Houry, M. Gohar, J. Deschamps, E. Tischenko, S. Aymerich, A. Gruss and R. Briandet, *Proceedings of the National Academy of Sciences*, 2012, **109**, 13088–13093.
- 3 L. J. Fauci and R. Dillon, *Annu. Rev. Fluid Mech.*, 2006, **38**, 371–394.
- 4 S. Mukhopadhyay, B. Allen and E. Brown, *Phys. Rev. E*, 2018, **97**, 052604.
- 5 M. E. Cates and J. Tailleur, *Annu. Rev. Condens. Matter Phys.*, 2015, **6**, 219–244.
- 6 N. Narinder, C. Bechinger and J. R. Gomez-Solano, *Phys. Rev. Lett.*, 2018, **121**, 078003.
- 7 C.-k. Tung, C. Lin, B. Harvey, A. G. Fiore, F. Ardon, M. Wu and S. S. Suarez, *Sci. Rep.*, 2017, **7**, 1–9.
- 8 K. Ishimoto and E. A. Gaffney, *Sci. Rep.*, 2018, **8**, 1–11.

- 9 C. Bechinger, R. Di Leonardo, H. Löwen, C. Reichhardt, G. Volpe and G. Volpe, *Rev. Mod. Phys.*, 2016, **88**, 045006.
- 10 K. Qi, E. Westphal, G. Gompper and R. G. Winkler, *Phys. Rev. Lett.*, 2020, **124**, 068001.
- 11 J. P. Binagia, A. Phoa, K. D. Housiadas and E. S. G. Shaqfeh, *J. Fluid Mech.*, 2020, **900**, A4.
- 12 K. D. Housiadas, J. P. Binagia and E. S. G. Shaqfeh, *J. Fluid Mech.*, 2021, **911**, A16.
- 13 G. Li and A. M. Ardekani, *Phys. Rev. Lett.*, 2016, **117**, 118001.
- 14 G. R. Fulford, D. F. Katz and R. L. Powell, *Biorheology*, 1998, **35**, 295–309.
- 15 Y. Nakayama and R. Yamamoto, *Phys. Rev. E*, 2005, **71**, 036707.
- 16 R. Yamamoto, J. J. Molina and Y. Nakayama, *Soft Matter*, 2021, **17**, 4226–4253.
- 17 J. J. Molina, Y. Nakayama and R. Yamamoto, *Soft Matter*, 2013, **9**, 4923–4936.
- 18 J. J. Molina and R. Yamamoto, *Mol. Phys.*, 2014, **112**, 1389–1397.
- 19 N. Oyama, J. J. Molina and R. Yamamoto, *Phys. Rev. E*, 2016, **93**, 043114.
- 20 N. Oyama, J. J. Molina and R. Yamamoto, *Eur. Phys. J. E Soft Matter*, 2017, **40**, 95.
- 21 N. Oyama, J. J. Molina and R. Yamamoto, *J. Phys. Soc. Jpn.*, 2017, **86**, 101008.
- 22 F. Fadda, J. J. Molina and R. Yamamoto, *Phys. Rev. E*, 2020, **101**, 052608.
- 23 Y. Matsuoka, Y. Nakayama and T. Kajiwara, *Soft Matter*, 2020, **16**, 728–737.
- 24 Y. Matsuoka, Y. Nakayama and T. Kajiwara, *J. Fluid Mech.*, 2021, **913**, A38.
- 25 J. S. Lintuvuori, A. Würger and K. Stratford, *Phys. Rev. Lett.*, 2017, **119**, 068001.
- 26 S. Mandal and M. G. Mazza, *Eur. Phys. J. E Soft Matter*, 2021, **44**, 64.
- 27 H. Tanaka and T. Araki, *Phys. Rev. Lett.*, 2000, **85**, 1338–1341.
- 28 M. A. Carrozza, M. A. Hulsen, M. Hütter and P. D. Anderson, *J. Non-Newtonian Fluid Mech.*, 2019, **270**, 23–35.
- 29 M. Hütter, M. A. Hulsen and P. D. Anderson, *J. Non-Newtonian Fluid Mech.*, 2018, **256**, 42–56.
- 30 M. J. Lighthill, *Commun. Pure Appl. Math.*, 1952, **5**, 109–118.
- 31 J. R. Blake, *J. Fluid Mech.*, 1971, **46**, 199–208.
- 32 T. Ishikawa and T. J. Pedley, *J. Fluid Mech.*, 2007, **588**, 437–462.
- 33 L. Zhu, E. Lauga and L. Brandt, *Phys. Fluids*, 2012, **24**, 051902.
- 34 G.-J. Li and A. M. Ardekani, *Phys. Rev. E*, 2014, **90**, 013010.
- 35 O. S. Pak and E. Lauga, *J. Eng. Math.*, 2014, **88**, 1–28.
- 36 H. Nganguia, K. Zheng, Y. Chen, O. S. Pak and L. Zhu, *Phys. Fluids*, 2020, **32**, 111906.
- 37 I. S. Vodop'yanov, A. G. Petrov and M. M. Shunderiyuk, *Fluid Dyn.*, 2010, **45**, 254–263.
- 38 H. Hasimoto, *J. Fluid Mech.*, 1959, **5**, 317–328.
- 39 X. Luo, M. R. Maxey and G. E. Karniadakis, *J. Comput. Phys.*, 2009, **228**, 1750–1769.
- 40 D. Rajagopalan, M. Arigo and G. H. McKinley, *J. Non-Newtonian Fluid Mech.*, 1996, **65**, 17–46.
- 41 C. Fernandes, S. A. Faroughi, O. S. Carneiro, J. M. Nóbrega and G. H. McKinley, *J. Non-Newtonian Fluid Mech.*, 2019, **266**, 80–94.
- 42 S. Wang and A. Ardekani, *Phys. Fluids*, 2012, **24**, 101902.